Langmuir

Article

pubs.acs.org/Langmuir

Study of Fluid and Transport Properties of Porous Anodic Aluminum Membranes by Dynamic Atomic Force Microscopy

Chu Wu,[†,‡] Hannah S. Leese,[∥] Davide Mattia,[∥] Raymond R. Dagastine,[†,§,⊥] Derek Y. C. Chan,*[,†,‡,#] and Rico F. Tabor*[,¶,†]

[†]Particulate Fluids Processing Centre, [‡]Department of Mathematics and Statistics, and [§]Department of Chemical and Biomolecular Engineering, University of Melbourne, Parkville 3010 Vic, Australia

[∥]Department of Chemical Engineering, University of Bath, Bath, U.K.

[⊥]Melbourne Centre for Nanofabrication, 151 Wellington Road, Clayton 3168, Australia

[#]Faculty of Life and Social Sciences, Swinburne University of Technology, Hawthorn 3122, Australia

Supporting Information

ABSTRACT: Recent work on carbon nanotubes (CNT) has focused on their potential application in water treatment as a result of their predicted and observed enhanced flow rates. Recent work on the lesser-known porous anodic alumina membranes (PAAMs) has also shown flow enhancement, albeit at only a fraction of what has been observed in CNTs. Despite their potential applications, little research has been conducted on PAAMs' hydrodynamic properties, and in this Article we present experimental results and theoretical models that explore the fluid flow behavior around and through these membranes. The experiments were conducted using an atomic force microscope (AFM) that pushed a solid silica particle against PAAMs that were characterized with different pore diameters. Furthermore, the PAAMs were classified as either closed or open, with the latter allowing fluid to pass through. The theoretical model developed to describe the experimental data incorporates Derjaguin–Landau–Verwey–Overbeek (DLVO) effects, cantilever drag, and hydrodynamic forces. By using the slip boundary condition for the hydrodynamic forces, we were able to fit the model to experimental findings and also demonstrate that the difference between closed and open PAAMs was negligible. The slip lengths did not correspond to any physical feature of the PAAMs, but our model does provide a simple yet effective means of describing the hydrodynamics for not only PAAMs but for membranes in general.

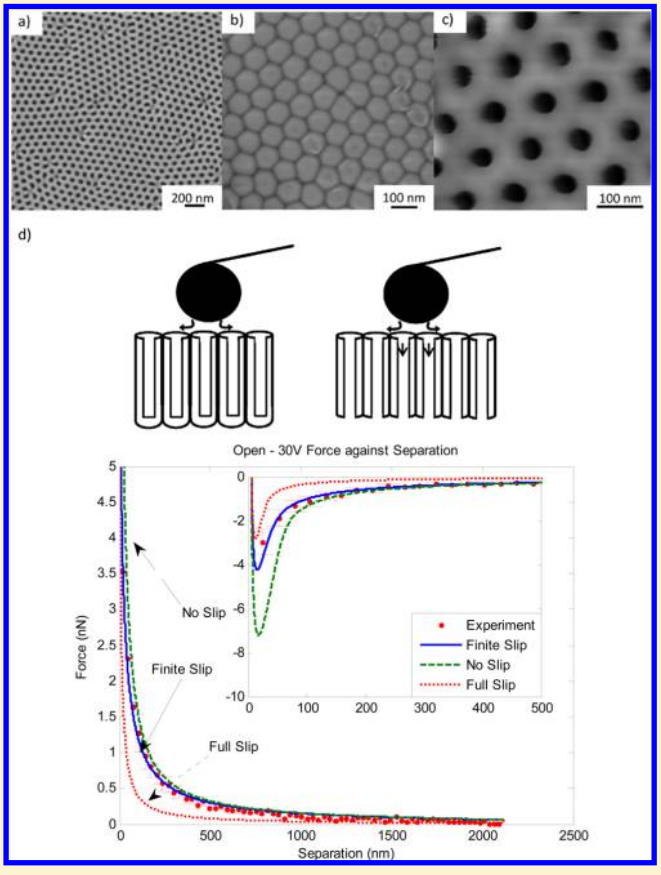

1. INTRODUCTION

Over the past few years, research into carbon nanotubes (CNTs) has garnered considerable research attention with the majority of this focus centering on their potential applications due to their remarkable physical properties. Their incredible strength is of interest in materials and mechanical engineering,[1] whereas their extremely high electrical conductivity is significant to electrical engineering disciplines.[2,3] Recent work has also focused on utilizing CNTs embedded in membranes for water treatment because of the low hydrodynamic resistance of such membranes observed in experimental studies and predicted in molecular simulation.[4−14] Recent work[13] has also demonstrated that hydrophilic nanochannels can exhibit low resistance to fluid flow. As a result of this, they are now being considered as a potential alternative to CNTs for use in water treatment. The experimental and theoretical work presented in

Received: April 3, 2013
Revised: June 6, 2013
Published: June 10, 2013

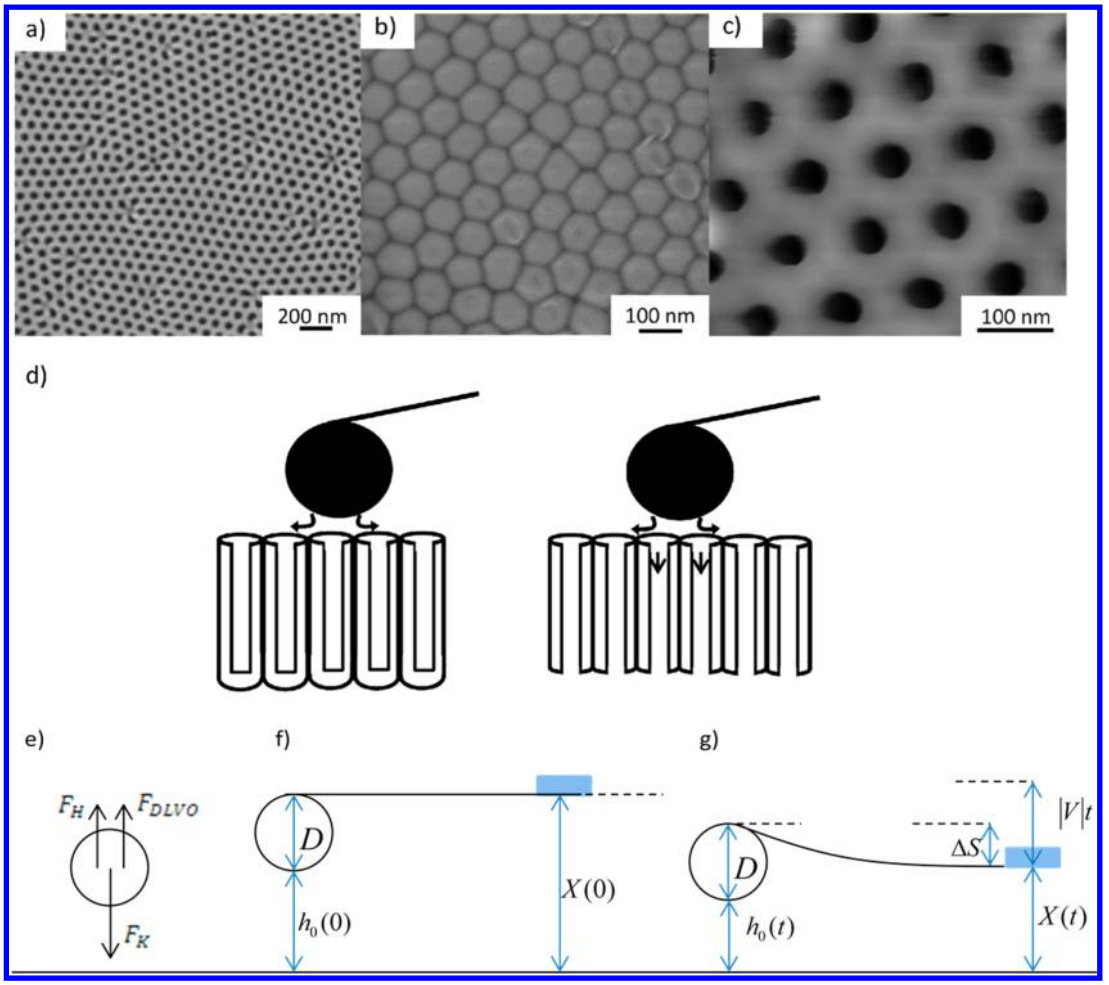

Figure 1. (a–c) FESEM of a porous anodic alumina membrane (PAAMs) at 40 V: (a) top surface that the silica particle was driven into for both the closed- and open-pore cases, (b) barrier oxide layer that caps the channels in closed-pore samples, and (c) tapping-mode AFM image after barrier oxide layer dissolution to give the open-pore case. (d) Schematic of a cross section of the closed-pore (left image) and open-pore (right image) systems. Note that the particle and pore sizes are not to scale. Physically, the particle has a diameter of around 20 μm whereas the pore size is considerably smaller, with diameters ranging from 10 to 100 nm depending on the anodization voltage. (e) Free-body diagram of the forces acting on the particle. (f and g) Diagrams of atomic force microscope (AFM) with the silica particle pushed against the PAAMs with respect to (f) the initial starting position of the system and (g) the case when the particle is being pushed against the surface that has caused the cantilever to deflect by ΔS.

this Article aims to describe the flow around and through these hydrophilic nanochannels, and the ideas and subsequent analysis presented here will be relevant to understanding the flow properties of membranes in general.

In this study, porous anodic alumina membranes (PAAMs) were used as the hydrophilic nanochannels. PAAMs have been utilized in many different applications, such as templates for synthesis procedures[14] and as material in fluid flow studies.[13] The PAAMs used in this study were fabricated at different anodization voltages, and this served to produce membranes with different pore diameters as shown in Figure 1a–c. At the same time, these membranes can be characterized as being either closed or open as illustrated in Figure 1d. The left-hand image is the closed case with the back of the PAAMs blocked, and the image on the right is an example of the open case where the back is now unblocked, thus allowing fluid to pass through.

The present experimental study uses the atomic force microscope (AFM) with a colloid probe to quantify fluid behavior near the PAAMs surface. The probe is made by gluing a colloidal particle to the tip of the AFM cantilever so as to provide a large surface area to interact with the membrane. This approach is known to be a very useful tool for investigating flow on the nanoscale through measuring the hydrodynamic forces.[15] Colloid probes can be driven toward the membrane surface at varying speeds to measure hydrodynamic interactions. This Article will present experimental results for and a theoretical analysis of several PAAMs with different pore diameters. Force measurements were conducted on both closed and open membranes to determine the potential effects of fluid drainage through membrane pores.

The theoretical model developed as part of this study incorporated van der Waals (vdW) and electric double layer (EDL) interactions considered in the Derjaguin–Landau–Verwey–Overbeek (DLVO) theory of colloidal forces.[16] The same DLVO modeling has been used successfully at different pH values and salt concentrations in AFM experiments on deformable surfaces.[17,18] The hydrodynamic interactions were modeled using Brenner's solution of a solid particle against a flat plate. This has been previously utilized in SFA experiments on film drainage of nonaqueous Newtonian fluids[19] as well as for non-Newtonian fluids containing nanoparticles.[20,21] The presence of the pores on the membrane surface for the open

dx.doi.org/10.1021/la401261z | Langmuir 2013, 29, 8969–8977

PAAMs leads to the possibility of flow passing through the membrane and is also incorporated into the modeling.

The presence of nanochannels in the PAAMs means that the membrane surface is not smooth but rather is covered with pores (Figure 1a). Because the nanochannels are hydrophilic, these pores will be will be filled when immersed in water, and thus the membrane surface is a solid with varying fractions of liquid regions.[22,23] Thus, fluid flowing across the surface will encounter a mixture of solid and liquid interfaces that in turn raises the possibility that the no-slip boundary condition (typically applied on uniformly solid surfaces) is not applicable for the membranes. Furthermore, for the open membranes the Stokes−Reynolds equation that can be used to derive the hydrodynamic forces for thin films[24] must be modified to account for flow through the membrane, and thus a new treatment of the hydrodynamic interaction is required.

The no-slip boundary condition assumes that the fluid velocity at the surface is equal to the surface velocity has been used successfully to model Couette and Hagen−Poiseuille flow as well as many other hydrodynamic and engineering systems on the macroscopic scale. It has also been used successfully to describe thin-film drainage behavior on the nanoscale for deformable surfaces.[25] However, the slip condition assumes that fluid velocity at the surface is different from the surface itself, and it has been argued that slip does occur for Newtonian fluids on the micro and nanoscales.[15]

The idea of a hydrodynamic slip boundary condition in which the tangential velocity of the fluid at an interface is proportional to the tangential stress was first proposed by Navier in 1823.[26,27] This idea has been revived as a convenient model to subsume complex flow conditions at surfaces that arise from surface structures or fluid granularity. For example, Bonaccurso et al. examined hydrodynamic slip using the AFM between a colloidal probe and surfaces with systematically increasing surface roughness.[28] The idea of hydrodynamic slip was proposed as a convenient way to capture this deviation between experimental results and the simple model of a smooth, solid no-slip surface. Zhu et al. used the AFM to study the hydrodynamic interactions between an OTS-coated silicon wafer and a borosilicate particle in di-*n*-octylphthalate fluid.[15] Deviations from the no-slip model in this unusual fluid/solid system were attributed to a slip length in the range of 24−31 nm at approach velocities of 10−80 μm/s.[15] More recent work by Gupta et al. made direct force measurements between surfaces with structured cylindrical posts arranged in a hexagonal array using a surface force apparatus (SFA)[29] where they modeled the hydrodynamic drainage behavior in terms of a deviation function from the no-slip case and employed a scaling analysis to describe the separation at the onset of the deviation.

However, it is clear that unless considerable effort is expended on accurately modeling the details of surface structures or fluid at interfaces (a task that may involve invoking a number of unknown parameters), the idea of slip can be useful in parametrizing this complex behavior if it can help predict the performance of industrial and technological processes such as flow through porous media, particle lubrication, and electroosmotic flow as well as better utilization of microfluidic and nanofluidic devices.[28]

2. EXPERIMENTAL SECTION

2.1. Fabrication of Porous Anodic Alumina Membranes (PAAMs). *2.1.1. Closed Pores.* A well-established two-step anodization process was carried out for the production of porous anodic alumina membranes (PAAMs).[13,30] High-purity (99.99%, 10 mm diameter) aluminum disks (Alfa Aesar) were first annealed in air at 500 °C for 60 min, degreased in acetone, and subsequently electropolished (1:4 v/v $HClO_4$/EtOH) prior to the first step of anodization. The pristine substrates were then anodized at 10−25 and 30−80 V in 0.5 M sulfuric acid and 0.3 M oxalic acid electrolytes, respectively, for 30 min. (See Table 1 for anodization conditions.) The alumina formed from the first step was then removed by wet chemical etching using a 1:1 mixture of 6 wt % H_3PO_4/1.8 wt % H_2CrO_4 at 60 °C for 20 min. Immediately after oxide removal, the substrate was anodized again (under the same conditions as in its first step) for 5 to 6 h for sulfuric acid and 10 to 12 h for the oxalic acid electrolyte.

Table 1. Properties and Anodization Conditions for Porous Anodic Alumina Membranes

anodization voltage (V)	electrolyte	pore diameter, d_P (nm)	interpore distance, D_C (nm)	porosity ϕ
10		14 ± 2	33 ± 3	0.11
20	0.5 M H_2SO_4, 0 °C	25 ± 4	54 ± 4	0.11
25		30 ± 4	64 ± 5	0.15
30		32 ± 3	94 ± 3	0.23
40	0.3 M $C_2H_2O_4$, 14 °C	44 ± 2	113 ± 2	0.18
50		52 ± 5	140 ± 3	0.17
60		59 ± 3	163 ± 6	0.11
70		99 ± 6	219 ± 7	0.32

2.1.2. Open Pores. To produce the open-pore membranes, two additional steps are added to the closed-pore procedure outlined above.[13] After obtaining a closed-pore sample, we removed the remaining aluminum layer after anodization with a 0.2 M $CuCl_2$/20% HCl mixture to expose the back layer of the alumina, which is known as the barrier oxide layer. To achieve PAAMs with open pores, the barrier oxide layer must be removed and the pores must be opened. Therefore, the PAAMs were exposed to hot (55 °C) H_3PO_4 for a period of 5−30 min (depending on the pore diameter). A Carl Zeiss XB1540 Gemini field emission scanning electron microscope was used to obtain images shown in Figure 1a,b, which show the top surface and the closed membrane structure. An AFM Veeco Multimode with a Nanoscope III controller was used to obtain Figure 1c, which presents images of the open-membrane structure after pore opening.

2.2. Force Measurements. To conduct dynamic force measurements on porous anodic alumina membranes (PAAMs), we used silicon nitride tipless cantilevers in the atomic force microscope (AFM). The cantilever spring constant was determined by the method of Hutter and Bechhoefer[31] and was in the range of 0.379 ± 0.076 N/m. The AFM measurements were performed on an Asylum MFP-3D AFM driven by an ARC1 controller. The AFM is also equipped with a linear variable differential transformer (LVDT) sensor in the *z*-movement direction to allow the direct detection of the cantilever *z* position during force measurements. This has been shown to be vital for accurate force−displacement measurements because the AFM piezo drive does not always vary linearly with the input voltage to within the required tolerance.[32]

The tipless cantilevers were loaded with approximately 20-μm-diameter silica particles. Smaller nanoparticles were not used because the particle size is proportional to the signal-to-noise ratio. The size and nature of the particle were selected to achieve the best balance between the sensitivity of flow and the signal-to-noise ratio. To do this, V-shaped cantilevers were mounted onto the cantilever holder with the aid of a high-magnification optical microscope (Nikon TE2000). The silica particles were distributed onto a glass slide alongside two-part glue (Arladite (F) "30 minute"). The tipless probe ends were dipped into the glue and then moved and lowered to pick up a silica particle.

dx.doi.org/10.1021/la401261z | *Langmuir* 2013, 29, 8969−8977

It was important to ensure that only one particle was attached to the probe (smaller particles could become attached to the end or the side of the cantilever, for instance) so that accurate force measurements could be taken. Once the particle probes had been left to dry, their structure was confirmed by observing the cantilever on its side under an optical microscope, and they were then mounted back into the cantilever holder. The holder had a skirt of Viton to protect the piezo and electronics from the fluids in the cell.

A range of PAAMs with different pore diameters (as described in Table 1) were used for the dynamic force measurements. Comparisons of the force curves between the closed and open pores were made. To ensure that there was no blocking of flow through the pores in the case of open PAAMs, the membranes were suspended across two glass coverslips and placed onto a glass Petri dish. To guarantee that there was no movement of the membrane when the measurements were taking place as the probe was driven into the surface, the coverslips were adhered to the bottom of the Petri dish with nail varnish. The membranes were also secured to the coverslips using this method. The measurements were performed in a 1 mM NaOH, pH 10 solution, and several areas of each membrane were tested at different velocities (from 20 to 100 μm/s).

3. THEORY

3.1. Particle Force Balance. The theoretical model can be obtained by considering the force balance on the cantilever particle. In the free-body diagram shown in Figure 1e, the three primary forces acting on the particle are the hydrodynamic force (F_H), the Derjaguin−Landau−Verwey−Overbeek force (F_{DLVO}), and the cantilever spring force (F_K). Because the Reynolds number of this system is very small, inertial forces can be neglected, and summing the forces in Figure 1e gives eq 1:

$$F_K = F_H + F_{DLVO} \tag{1}$$

3.2. Spring Force and Cantilever Drag. Figure 1f,g shows a schematic diagram of the atomic force microscope (AFM). Here, $h_0(t)$ is the separation between the particle and the substrate, and $h_0(0)$ is the initial separation. D is the particle diameter, ΔS is the cantilever deflection, $X(t)$ is the cantilever position at time t, and V is the recorded linear variable differential transformer (LVDT) velocity. The AFM experiments were conducted at velocities of around 20−100 μm/s, and as a result, the cantilever may be subjected to hydrodynamic drag. Thus the apparent force measured by the AFM (F_{app}) will be a combination of the force on the particle and the cantilever drag. For this model, it is assumed that drag is directly proportional to the product of the cantilever velocity, fluid viscosity, and a drag constant term.[33] Through Figure 1f,g, it is possible to relate $h_0(t)$ to the known parameters of V and t recorded from the AFM.

$$F_{app} = F_K + F_{drag} = F_K + C\mu\frac{dX}{dt} \tag{2}$$

The C term is the aforementioned drag constant, and μ is the fluid viscosity. The apparent force can be linked to the cantilever deflection ΔS through Hooke's law, with K being the spring constant. Again using Figure 1f,g, we can relate the force experienced by the particle to the AFM parameters to form eq 3

$$F_K = K(h_0(t) - h_0(0) + |V|t) - C\mu\frac{dX}{dt} \tag{3}$$

with $h_0(0)$ being the initial separation, C being the drag constant, and $|V|$ being the absolute velocity. In our model, a positive velocity occurs when the particle moves away from the membrane. The cantilever spring constant was measured to be 0.379 ± 0.076 N m^{-1}. The drag constant was approximated in the model as 4×10^{-3} m, which is of the same order as those in previous studies.[33] The initial separation cannot be measured accurately, and this value was determined through matching the experimental and theoretical force peaks.

3.3. Derjaguin−Landau−Verwey−Overbeek (DLVO) Forces. The Derjaguin−Landau−Verwey−Overbeek (DLVO) component consists of both the electric double layer (EDL) and van der Waals (vdW) forces. Both components are modeled through Derjaguin's approximation that states that the force between a spherical colloidal particle (radius R) and a flat plate is $2\pi R$ multiplied by the interaction energy per unit area between two semi-infinite surfaces.[16]

$$F_{DLVO} = 2\pi R W_{EDL} + 2\pi R W_{vdW} \tag{4}$$

The van der Waals interaction energy per unit area (W_{vdW}) is given by

$$W_{vdW} = -\frac{A}{12\mu h^2} \tag{5}$$

Here, A is the Hamaker constant for a silica−water−alumina system that was approximated to be 1.4×10^{-20} J using the approximation of the nonretarding Hamaker constant as outlined in Israelachvili.[16] The interaction energy for the EDL (W_{EDL}) is found by first implicitly solving the Poisson−Boltzmann equation to determine the EDL disjoining pressure using a method described by Chan et al.[34] The resulting disjoining pressure had to be integrated numerically because this solution was not in closed form and this will result in W_{EDL}. Substituting this result and eq 5 into eq 4 will yield the following:

$$F_{DLVO} = 2\pi R W_{EDL} - \frac{RA}{6h^2} \tag{6}$$

The aqueous solution used in the experiments consisted of 0.1 M NaOH at pH 11. The high pH was set deliberately to ensure that the surface potential would be very high. For the modeling, this was assumed to be around −100 mV and is consistent with observations from previous studies on the pH-controlled coalescence of deformable surfaces.[35]

3.4. Hydrodynamic Forces: Closed Pores. For our system, the hydrodynamic force for a Newtonian fluid with a dynamic viscosity of μ can be found through solving the Stokes−Reynolds equation as expressed in eq 7

$$\frac{dh}{dt} = \frac{1}{12\mu r}\frac{\partial}{\partial r}\left(rH\frac{\partial P}{\partial r}\right) \tag{7}$$

$$H = \begin{cases} h^3 & \text{no slip} \\ h^3\left(\dfrac{h + 4b_0}{h + b_0}\right) & \text{finite slip} \\ 4h^3 & \text{full slip} \end{cases} \tag{8}$$

where b_0 is the slip length and analytical solutions to eq 7 are given in eq 9.[36] The equation is essentially Stokes flow with a correction term λ that takes into account the presence of the wall. The correction term is dependent on whether the system is no slip ($b_0 = 0$), finite slip (where b_0 equals some finite number), or infinite slip (b_0). The solution to all of these cases is shown in eq 9:

dx.doi.org/10.1021/la401261z | Langmuir 2013, 29, 8969−8977

$$F_H = 6\pi R^2 \frac{dh}{dt}\lambda \tag{9a}$$

$$\lambda = \begin{cases} \frac{1}{h} & \text{no slip} \\ \frac{1}{4h} + \frac{3}{32{b_0}^2}\left[(h+4b_0)\log\left(\frac{h+4b_0}{h}\right) - 4b_0\right] & \text{finite slip} \\ \frac{1}{4h} & \text{infinite slip} \end{cases} \tag{9b}$$

3.5. Hydrodynamic Forces: Open Pores. In the open-pore PAAMs case, the Stokes–Reynolds equation (eq 7) must be modified to accommodate the possibility of fluid passing through the membrane, as observed in previous wetting and permeability studies using the same materials.[22,23] The derivation for this is outlined in the Supporting Information, but the modified Stokes–Reynolds equation is presented below

$$\frac{dh}{dt} = \frac{1}{12\mu r}\frac{\partial}{\partial r}\left(rH\frac{\partial P}{\partial r}\right) - \frac{\phi D^2 P}{32\mu L} \tag{10}$$

where ϕ and L are the porosity and thickness of the PAAMs, respectively. Unlike the closed-pore PAAMs, there is no closed-form analytical solution to eq 10, so a perturbation solution of first order was sought. The perturbation solutions for the no-slip and infinite-slip cases are presented in eq 11 with their derivations found in the Supporting Information

$$F_H = 6\pi\mu R^2 \frac{dh}{dt}\lambda \tag{11a}$$

$$\lambda = \begin{cases} \frac{1}{h} - \frac{\mu R\alpha}{h^2} & \text{no slip} \\ \frac{1}{4h} - \frac{\mu R\alpha}{16h^2} & \text{infinite slip} \end{cases} \tag{11b}$$

where $\alpha = (\phi D^2)/(32\mu L)$. If α is equal to zero (representing a membrane with no pores), then the no-slip and infinite-slip solutions in eq 11 becomes equivalent to the corresponding no-slip and infinite-slip solutions in eq 9. The α term is typically on the order of 10^{-10} m^3/Ns, so the right-hand perturbation term in eq 11 is very small. Thus, the difference between eqs 11 and 9 for the no-slip and infinite-slip cases is insignificant, with the perturbations becoming important only at very small separations. No perturbation solution to the finite-slip case for eq 10 was found, but it will lie somewhere between the no-slip and infinite-slip solutions expressed in eq 11 and can be approximated by the finite-slip solution in eq 9 because the difference between the open and closed cases is expected to be negligible.

3.6. Combining the Equations. The equation of motion describing particle–membrane separation $h_0(t)$ in the center of the particle is found by combining eqs 1, 3, 6, 9, and 11 to give eq 12:

$$K(h_0(t) - h_0(0) + |V|t) - C\mu V = -6\pi R^2 \frac{dh}{dt}\lambda + 2\pi R W_{EDL} - \frac{RA}{6h^2} \tag{12}$$

Once the experimental LVDT velocity V is given, eq 12 can be solved numerically.

4. RESULTS AND DISCUSSION

4.1. Flat Alumina Surfaces. Control experiments were conducted initially on a flat alumina disc. The no-slip boundary conditions were used in the modeling and are presented as the solid curve in Figure 2, where the atomic force microscope (AFM) cantilever was driven at nominal speeds of around 20 μm/s. The main plot shows the repulsive force against separation during the approach stage, and the attractive hydrodynamic force during retraction is shown in the inset. The no-slip model fits the experimental results (dots with error bars) accurately, though there is a slight deviation at the force minimum on retraction. This may be caused by unknown surface features such as localized surface roughness that interferes with the probe particle at close separations.

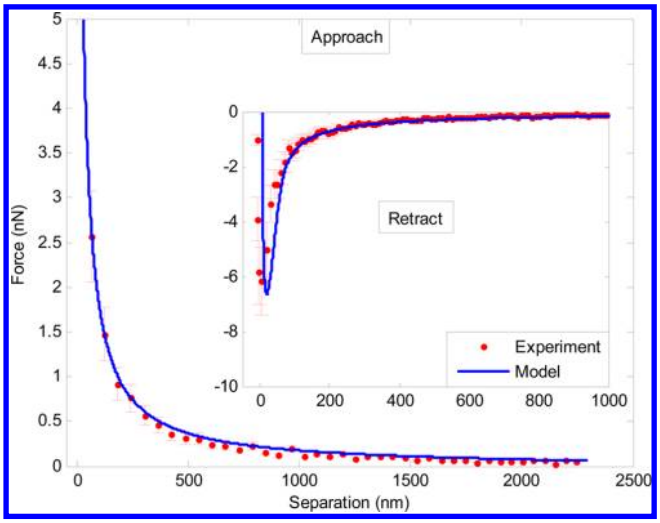

Figure 2. Force against separation for a flat alumina disc driven at a nominal velocity of 20 μm/s using a drag constant of 0.004 m with a 20-μm-radius silica particle. A Hamaker constant of 1.4×10^{-20} J and a surface potentials of −100 mV were used in the model. The experiment was conducted in 0.1 M NaOH solution at a pH of 11.

4.2. Closed Pores. A comparison of the no-slip, infinite-slip, and finite-slip model against the experimental closed-pore PAAMs anodized at 40 V with a pore diameter of 40 ± 2 nm is shown in Figure 3 with a nominal speed of around 40 μm/s. For these systems, the pores were closed off at the back so that water fills the pores but cannot pass through (Figure 1d). The no-slip (dashed) and infinite-slip (dotted) force curves lie above and below the experimental results, respectively. This suggests that a slip model is needed, and this is indicated by the solid curve in Figure 3 where a slip length (b_0) of 80 nm was used.

The incorporation of slip length into our model provides a simplistic but convenient way to summarize the variations of the measured hydrodynamic forces for membranes with different surface structures. Clearly an ab initio prediction of hydrodynamic flow conditions under the differing surface morphologies of the membranes is a challenging task. Our goal is to seek a simple relationship between membrane morphology and flow conditions.

This relationship is highlighted in Figure 4, where large pore diameters have corresponding larger slip lengths. However, there is some variability in the model slip length due to uncertainties with the measured force, which as mentioned earlier was around 0.379 ± 0.076 N/m. The height and width

dx.doi.org/10.1021/la401261z | Langmuir 2013, 29, 8969–8977

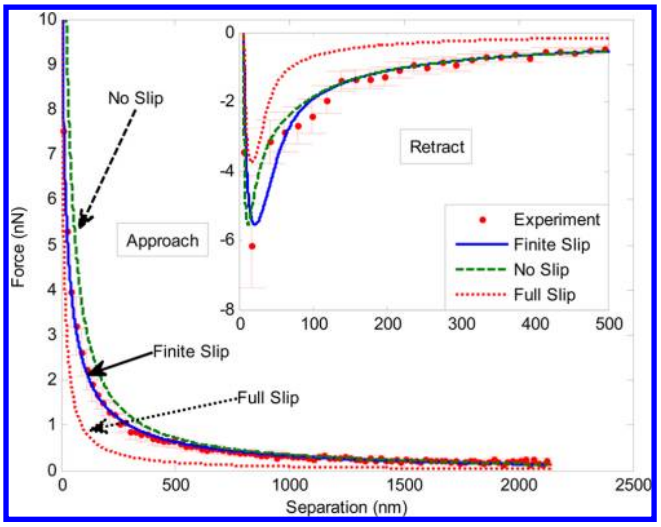

Figure 3. Force against separation curves for porous anodic alumina membrane (PAAMs) with closed pores produced at an anodization voltage of 40 V with a pore diameter of 44 ± 2 nm driven at a nominal speed of 40 μm/s with a 20-μm-radius silica particle. A Hamaker constant of 4×10^{-20} J and a surface potential of −100 mV were used in the model. The experiment was conducted in 0.1 M NaOH solution at pH 11.

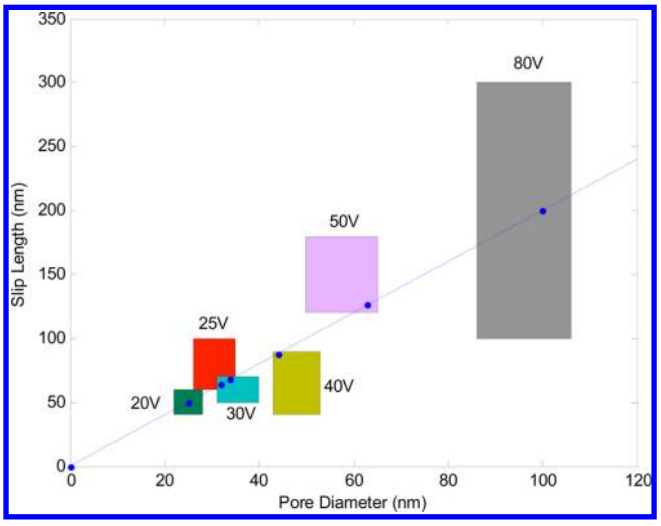

Figure 4. Measured pore diameter corresponding to model slip lengths (b_0) for different porous anodic alumina membranes (PAAMs) with closed pores produced at differing anodization voltages. The dots mark the data points used to find the linear least-squares fit marked by the solid line.

of the rectangles in Figure 4 represent the range of slip lengths and pore diameters that lie within the experimental uncertainties. For slip lengths, this was determined through selecting the largest and smallest slip lengths whereby the model will lie within the uncertainties of the experimental force curves. The uncertainty in the pore diameters was found by analyzing several areas of a membrane using Image J software to calculate the standard deviation of the pore diameters. Thus the resulting rectangles represent all of the possible combinations of slip lengths and pore diameters that lie within the experimental uncertainty. Furthermore, it is possible to pass a linear least-squares regression through all of the rectangles as marked by the line in Figure 4. This particular line also passes through the origin and is consistent with observations in Figure 2 where the model required the no-slip condition to fit the flat PAAMs experimental data. However, the pore diameter is considerably smaller than the slip lengths used in the modeling, and this disparity in length scales suggests that there may be some unknown factors contributing to the slip behavior. Nonetheless, an ab initio derivation of this system will be extremely difficult, and using the slip model provides a simple yet reasonably accurate description of the system.

4.3. Open Pores. A comparison of the nonperturbation solution in eq 9 and the perturbations solution in eq 11 shows that the two equations for the no-slip and full-slip cases differ only by the term on the right side of eq 11 that contains the α variable. The expression $\mu R\alpha/h^2$ is considerably smaller than 1 for values of $h_0(t)$ that are greater than 5 nm. Thus the difference between eqs 9 and 11 for the no-slip and infinite-slip cases is negligible.

This is illustrated in Figure 5, where comparisons of the perturbation and nonperturbation solutions for the no-slip and

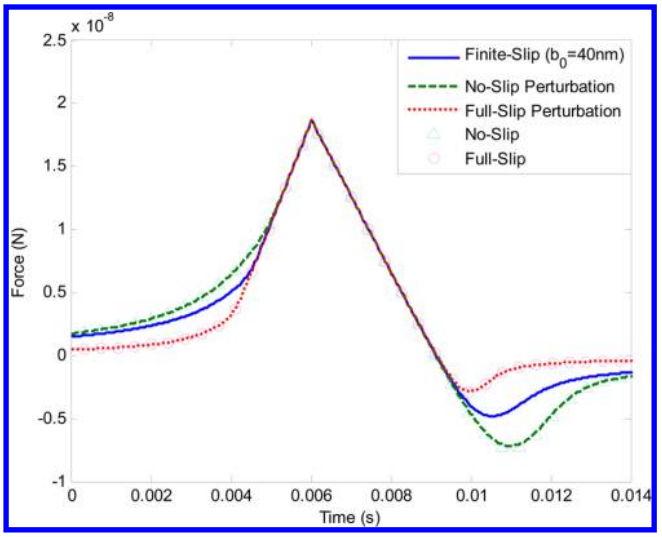

Figure 5. Comparison of the perturbation and nonperturbation analytical solutions for open porous anodic alumina membranes (PAAMs) at an anodization voltage of 40 V with a pore diameter of 44 ± 2 nm at a nominal speed of 20 μm/s. The dashed and dotted lines are the no-slip and full-slip perturbation solutions, respectively. The triangles and circles are the no-slip and full-slip nonperturbation solutions, respectively. The solid curve is the finite-slip nonperturbation solution.

infinite-slip cases are shown. The nonperturbation solution curves (triangles and circles for no slip and infinite slip, respectively) lie directly on those for the corresponding perturbation solutions (dashed and dotted lines for no slip and infinite slip, respectively). No perturbation solution for the finite-slip case was found. However, it is expected to lie somewhere between the no-slip and infinite-slip perturbation solutions that are known. Furthermore, because the deviations between the nonperturbation and perturbation solutions are negligible, it is possible to use the former as an approximation for the latter at finite-slip lengths.

To highlight this further, we show in Figure 6 the theoretical breakdown of the different pressures acting at the center of the silica particle probe calculated using the model. The maximum total pressure is approximately 170 kPa, which is outside the vertical scale of Figure 6, and by far the largest contribution is from the electric double layer (EDL) repulsion. As the particle

dx.doi.org/10.1021/la401261z | Langmuir 2013, 29, 8969−8977

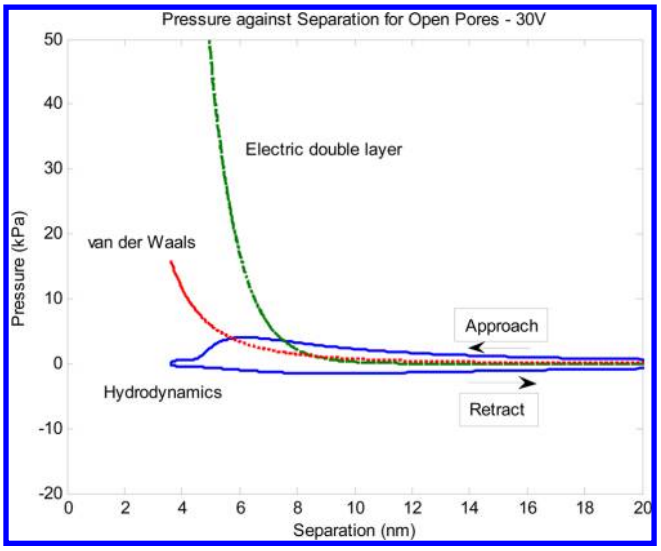

Figure 6. Breakdown of the pressure in the center of the colloid particle calculated from the theoretical model at a nominal speed of 20 μm/s. Solid, dashed, and dotted lines represent the hydrodynamics, electric double layer, and van der Waals pressure, respectively.

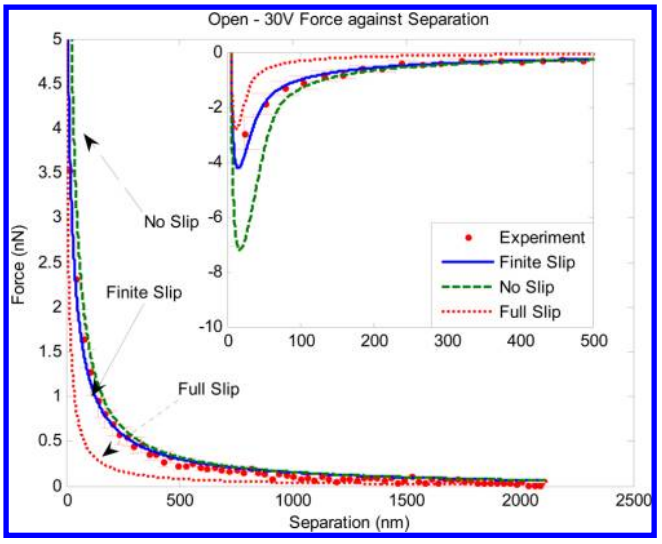

Figure 7. Force against separation for open-pore porous anodic alumina membranes (PAAMs) at an anodization voltage of 30 V with a pore diameter of 32 ± 3 nm at a nominal speed of 20 μm/s with a 20-μm-radii silica particle. A Hamaker constant of 4×10^{-20} J and a surface potential of −100 mV were used in the model. The experiment was conducted in 0.1 M NaOH solution at a pH of 11. Experimental data are represented by the dots with error bars. The dashed and dotted curves are the no-slip and full-slip perturbation solutions, respectively. The solid curve is the finite-slip approximation (b_0 = 40 nm) of the experimental results using the nonperturbation finite-slip model.

approaches the surface, the separation decreases, but at the same time, the velocity also decreases as a result of the increasing repulsion caused by the Derjaguin−Landau−Verwey−Overbeek (DLVO) forces. According to eqs 9 and 11, the hydrodynamic force and hence the hydrodynamic pressure are inversely proportional to the separation but directly proportional to the velocity. Therefore, as the particle approaches the PAAMs surface, the velocity approaches zero and the hydrodynamic pressure constitutes only a small part of the total pressure with values typically below 20 kPa. The small hydrodynamic pressure may not be large enough to cause significant flow through the pores. Lee et al. found that significant flow through the PAAMs required a hydrodynamic pressure on the order of 100 kPa.[13] Although it is possible that there is some flow through the open pores, the very small hydrodynamic pressure suggests that it is not the main contributor to the resulting force curves.

Figure 7 shows the experimental force curves (dots with error bars) for open-pore PAAMs anodized at 30 V; the PAAMs have a relatively small average pore diameter of 32 ± 3 nm. The dashed and dotted lines are the no-slip and infinite-slip perturbation models, respectively, and as in Figure 4, these lines bracket the experimental results, thus indicating the need to introduce slip. The finite-slip model (solid curve) is approximated using the closed-pore nonperturbation solution and again matches the experiments on approach though it deviates slightly on retraction where the experimental minimum is deeper than that in the model. As in Figure 3, it is believed that the localized surface roughness may be the cause for the deviation.

In some samples of open-pore PAAMs, particularly at large pore sizes, we measure almost no forces until the colloid probe comes into hard contact (constant compliance) with the membrane. We attribute such results to the fact that the final fabrication step in opening the pores (section 2.1.2) can result in PAAMs surfaces that are considerably rougher than their closed-pore counterparts. As a result, the colloid probe tends to interact with the tall asperities of the rough membrane surface. This occurs when the rest of the membrane surface is still well separated from the colloid probe with the result that no interactions are detected.

5. CONCLUSIONS

By using the atomic force microscope (AFM) to probe the surface of porous anodic alumina membranes (PAAMs) and modeling the experimental results, we were able to gain greater insight into the flow characteristics of these membranes. For closed PAAMs, the no-slip boundary condition is no longer applicable because the surface is no longer solid but rather a mixture of water and alumina. Assuming slip enables the theoretical model to match the experimental results. The slip lengths are found to be proportional to the PAAM pore diameter, and the no-slip boundary condition is expected to hold for a completely flat, featureless surface. In the absence of an ab initio model to quantify the hydrodynamic complexities of the porous morphology of such porous membranes, the slip model provides a simple and convenient way to summarize the main hydrodynamic characteristics.

The experimental results for the open-channel PAAMs did not differ significantly from those of the closed PAAMs at small pore diameter. However the open nanochannels raise the possibility that fluid can pass through the membrane via the nanochannels, and the Stokes−Reynolds equation must be modified to accommodate for this. A perturbation solution for the hydrodynamic pressure was found, which suggests that there is little difference between the two cases and also indicates that very little flow is expected to pass through the membrane at these diameters. Thus for these cases it is possible to employ the no-slip boundary condition to describe flow parallel to any membrane surface (not just PAAMs) if the pressure perpendicular to the membrane is small. At larger pore sizes, surface roughness effects dominate the force measure-

dx.doi.org/10.1021/la401261z | Langmuir 2013, 29, 8969−8977

ment experiments and preclude detailed probing of the hydrodynamic transport through the membrane pores.

■ ASSOCIATED CONTENT

Supporting Information

Derivations of flow through porous anodic alumina membranes, the modified Stokes−Reynolds equation, and the perturbation solution of the modified Stokes−Reynolds equation. Discussion of the flow between two surfaces. This material is available free of charge via the Internet at http://pubs.acs.org

■ AUTHOR INFORMATION

Corresponding Author

*E-mail: D.Chan @unimelb.edu.au; Rico.Tabor@monash.edu.au

Present Address

[¶]School of Chemistry, Monash University, Clayton 3168, Australia.

Author Contributions

C.W. and H.S.L. contributed equally to this work.

Notes

The authors declare no competing financial interest.

■ ACKNOWLEDGMENTS

This work is supported in part by an Australian Research Council Discovery Project grant. C.W. is supported by an Australian Postgraduate Award. Infrastructure support provided by the Particulate Fluids Processing Centre is gratefully acknowledged. We also acknowledge the UK EPSRC (EP/6045798/1 and EP/J015504/1) for funding and the Microscopy and Analysis Suite at the University of Bath and NanoAccess in Cardiff, EPSRC (EP/F056745/1).

■ REFERENCES

(1) Dalton, A. B.; Collins, S.; Muñoz, E.; Razal, J. M.; Ebron, V. H.; Ferraris, J. P.; Coleman, J. N.; Kim, B. G.; Baughman, R. H. Super-tough carbon-nanotube fibres. *Nature* **2003**, *423*, 703.

(2) Mattia, D.; Rossi, M.; Ye, H.; Gogotsi, Y. In Situ Fluid Studies in Carbon Nanotubes with Diameters Ranging from 1 to 500 nm. *Proceedings of the 5th IASME/WSEAS International Conference on Fluid Mechanics and Aerodynamics*; Athens, 2007; pp 294−296.

(3) Ebbesen, T.; Lezec, H.; Hiura, H.; Bennett, J.; Ghaemi, H.; Thio, T. Electrical conductivity of individual carbon nanotubes. *Nature* **1996**, *382*, 54−56.

(4) Supple, S.; Quirke, N. Molecular dynamics of transient oil flows in nanopores I: imbibition speeds for single wall carbon nanotubes. *J. Chem. Phys.* **2004**, *121*, 8571−8579.

(5) Supple, S.; Quirke, N. Rapid imbibition of fluids in carbon nanotubes. *Phys. Rev. Lett.* **2003**, *90*, 214501.

(6) Joseph, S.; Aluru, N. R. Why are carbon nanotubes fast transporters of water? *Nano Lett.* **2008**, *8*, 452−458.

(7) Thomas, J.; McGaughey, A. Water flow in carbon nanotubes: transition to subcontinuum transport. *Phys. Rev. Lett.* **2009**, *102*, 184502.

(8) Thomas, J. A.; Mcgaughey, A. J. H. Reassessing fast water transport through carbon nanotubes. *Nano Lett.* **2008**, *8*, 2788−2793.

(9) Whitby, M.; Cagnon, L.; Thanou, M.; Quirke, N. Enhanced fluid flow through nanoscale carbon pipes. *Nano Lett.* **2008**, *8*, 2632−2637.

(10) Majumder, M.; Chopra, N.; Andrews, R.; Hinds, B. J. Enhanced flow in carbon nanotubes. *Nature* **2005**, *438*, 44.

(11) Corry, B. Water and ion transport through functionalised carbon nanotubes: implications for desalination technology. *Energy Environ. Sci.* **2011**, *4*, 751.

(12) Kannam, S. K.; Todd, B. D.; Hansen, J. S.; Daivis, P. J. How fast does water flow in carbon nanotubes? *J. Chem. Phys.* **2013**, *138*, 094701.

(13) Lee, K. P.; Leese, H.; Mattia, D. Water flow enhancement in hydrophilic nanochannels. *Nanoscale* **2012**, *4*, 2621−2627.

(14) Martin, C. R. Nanomaterials: a membrane-based synthetic approach. *Science* **1994**, *266*, 1961−1966.

(15) Zhu, L.; Attard, P.; Neto, C. Reliable measurements of interfacial slip by colloid probe atomic force microscopy. I. Mathematical modeling. *Langmuir* **2011**, *27*, 6701−11.

(16) Israelachvili, J. *Intermolecular and Surface Forces*, 2nd ed.; Academic Press: London, 1991; pp 161−164.

(17) Tabor, R. F.; Wu, C.; Lockie, H.; Manica, R.; Chan, D. Y. C.; Grieser, F.; Dagastine, R. R. Homo- and hetero-interactions between air bubbles and oil droplets measured by atomic force microscopy. *Soft Matter* **2011**, *7*, 8977.

(18) Tabor, R. F.; Wu, C.; Grieser, F.; Chan, Y. C.; Dagastine, R. R. Non-linear and cyclical collisions between drops and bubbles: using AFM to understand droplet interactions in micro-scale flows. *Soft Matter* **2013**, *9*, 2426−2433.

(19) Chan, D. Y. C.; Horn, R. G. The drainage of thin liquid films between solid surfaces. *J. Chem. Phys.* **1985**, *83*, 5311−5324.

(20) James, G. K.; Walz, J. Y. Hydrodynamic force on a microparticle approaching a wall in a nanoparticle dispersion: observation of a separation-dependent effective viscosity. *Langmuir* **2012**, *28*, 92−103.

(21) Tulpar, A.; Walz, J. Y. Simultaneous measurement of structural and hydrodynamic forces between colloidal surfaces in complex fluids. *Colloids Surf., A* **2007**, *300*, 268−280.

(22) Leese, H.; Bhurtun, V.; Lee, K. P.; Mattia, D. Wetting behaviour of hydrophilic and hydrophobic nanostructured porous anodic alumina. *Colloids Surf., A* **2013**, *420*, 53−58.

(23) Ran, C.; Ding, G.; Liu, W.; Deng, Y.; Hou, W. Wetting on nanoporous alumina surface: transition between Wenzel and Cassie states controlled by surface structure. *Langmuir* **2008**, *24*, 9952−9955.

(24) Chan, D. Y. C.; Klaseboer, E.; Manica, R. Theory of non-equilibrium force measurements involving deformable drops and bubbles. *Adv. Colloid Interface Sci.* **2011**, *165*, 70−90.

(25) Dagastine, R. R.; Manica, R.; Carnie, S. L.; Chan, D. Y. C.; Stevens, G. W.; Grieser, F. Dynamic forces between two deformable oil droplets in water. *Science* **2006**, *313*, 210−213.

(26) Navier, C. L. M. H. Mémoire sur les lois du mouvement des fluids. *Mem. Acad. Sci. Inst. FR* **1823**, *6*, 389−416.

(27) Navier, C. L. M. H. Mémoire sur les lois du mouvement des fluids. *Mem. Acad. Sci. Inst. FR* **1823**, *6*, 432−436.

(28) Bonaccurso, E.; Butt, H.-J.; Craig, V. S. Surface roughness and hydrodynamic boundary slip of a newtonian fluid in a completely wetting system. *Phys. Rev. Lett.* **2003**, *90*, 1−4.

(29) Gupta, R.; Fréchette, J. Measurement and scaling of hydrodynamic interactions in the presence of draining channels. *Langmuir* **2012**, *28*, 14703−14712.

(30) Masuda, H.; Fukuda, K. Ordered metal nanohole arrays made by a two-step replication of honeycomb structures of anodic alumina. *Science* **1995**, *268*, 1466−1468.

(31) Hutter, J. L.; Bechhoefer, J. Calibration of atomic-force microscope tips. *Rev. Sci. Instrum.* **1993**, *64*, 1868.

(32) Manor, O.; Vakarelski, I. U.; Stevens, G. W.; Grieser, F.; Dagastine, R. R.; Chan, D. Y. C. Dynamic forces between bubbles and surfaces and hydrodynamic boundary conditions. *Langmuir* **2008**, *24*, 11533−11543.

(33) Dagastine, R. R.; Webber, G. B.; Manica, R.; Stevens, G. W.; Grieser, F.; Chan, D. Y. C. Viscosity effects on hydrodynamic drainage force measurements involving deformable bodies. *Langmuir* **2010**, *26*, 11921−11927.

(34) Chan, D. Y. C.; Healy, T. W.; Supasiti, T.; Usui, S. Electrical double layer interactions between dissimilar oxide surfaces with charge regulation and Stern-Grahame layers. *J. Colloid Interface Sci.* **2006**, *296*, 150−158.

(35) Tabor, R. F.; Chan, D. Y. C.; Grieser, F.; Dagastine, R. R. Anomalous stability of carbon dioxide in pH-controlled bubble coalescence. *Angew. Chem., Int. Ed.* **2011**, *50*, 3454−3456.
(36) Vinogradova, O. I. Drainage of a thin liquid film confined between hydrophobic surfaces. *Langmuir* **1995**, *11*, 2213−2220.